4. Electric Fields in Cosmic Plasma

Electric fields play a crucial role in cosmic plasmas. Electric fields can accelerate charged particles to high energies and cause currents to flow, generate and "unfreeze" magnetic fields in plasmas, cause plasma to pinch into filaments, separate chemical elements, and initiate the collapse of plasma to the condensate and neutral state of matter.

Until fairly recent times, electric fields were thought impossible, first in space (because the conductivity σ was thought to be zero), and then in cosmic plasma (because the conductivity σ was thought to be infinite and the plasma thought to be uniform). For these reasons, other mechanisms were sought to explain the existence of highly-relativistic charged particles which, in terrestrial laboratories, are produced only by accelerators with high potential gradients (i.e., electric fields).

The discovery of magnetic-field-aligned ("parallel") electric fields in space above the aurora has profoundly changed our concepts of particle energization and plasma dynamics in the magnetosphere. It may also have far-reaching implications for the understanding of other space and astrophysical plasmas. The parallel electric field itself is hard to measure directly, but concurrent evidence of its existence has come from measured particle distributions—electrons as well as ions—both outside and inside the regions of parallel electric fields. Thus the existence of parallel electric fields with voltages of several kilovolts is now beyond doubt, but their distribution in space is still incompletely known.

Section 4.1 briefly mentions how electric fields occur. The methods of measuring electric fields are discussed (Section 4.2), followed by the mechanisms that lead to parallel electric fields in the magnetosphere (Section 4.3). A review of the data obtained from satellite and rocket measurements is then presented in Section 4.4. The fruit of these efforts is knowledge that is fundamental to our understanding of plasma-related phenomena in the rest of the universe, which will forever lie beyond the reach of *in situ* measurement. Sections 4.5–4.6 start the application of this knowledge to these regions of the universe.

4.1 Electric Fields

Maxwell–Hertz–Heaviside's equations (1.1) and (1.3),

$$\nabla \times \mathbf{E} = -\frac{\partial \mathbf{B}}{\partial t}$$

$$\nabla \cdot \mathbf{E} = \rho / \varepsilon_0 = -\frac{e}{\varepsilon_0}(n_e - n_i)$$

tell us that electric fields derive from either of two mechanisms: time-varying magnetic fields or charge separation. These two equations are deceptively simple and convey no information about the multitude of mechanisms whereby a time-varying magnetic field arises or charges separate. Two examples of the former are given in Sections 3.5.2 and 3.5.3. Charge separation can occur from from plasma instabilities (Section 1.7.3), gyrations in a magnetic field, magnetic field and temperature gradients, diffusion, drifts, and radiation forces. Intense, high-frequency radiation nearly always produces free charges in dielectrics which lead to potential gradients $\nabla\phi$ from which an electric field $\mathbf{E} = -\nabla\phi$ derives.

In electromagnetism, understanding the physical system under study is incomplete without the knowledge of the electric field. For this reason, field maps of $\mathbf{E}$ are highly sought after in laboratory and space plasmas. However, in contrast to the relative simple measurement of magnetic fields, electric fields are far harder to measure.

4.2 Measurement of Electric Fields

A wide variety of techniques for measuring electric fields with strengths ranging from millivolts per centimeter to megavolts per centimeter have been developed. In pulsed energy applications, *E*-dot (or *V*-dot) probes, resistive dividers, and electrooptic crystals are used. In space plasmas, spherical double probes, radar, electron beams, and ion detectors find employment. The mapping of electric fields in space plasma is also possible by following the motions of rocket released ionized barium clouds, observing the paths that whistler waves take, and from the convection of ions in space regions. Rydberg states may also be used for the measurement of electric fields in space and astrophysical plasmas [Garscadden 1986].

V-Dot Detectors. A *V*-dot detector is the electric field analog to the *B*-dot detector (Chapter 3). This detector can be as simple as a chopped-off coaxial cable with its tip exposed to the voltage that is to be measured. A slightly modified design uses a coaxial cable with a small metal sphere or a plate attached to increase sensitivity. The exposed tip can then be inserted through one electrode or conductor into the medium in which an electric field is present. The detector will capacitive couple to the opposite electrode or conductor, producing a signal proportional to the area of the detector times the rate of change of the voltage between conductor elements.

Figure 4.1 illustrates how a *V*-dot detector is used to measure the field component normal to the probe plate. The current density $\mathbf{J}$ consists of two parts: a conduction current dependent on the field $\mathbf{E}$ and the conductivity of the medium σ, and a displacement current that is proportional to the permittivity ε,

$$\mathbf{J} = \mathbf{J}_{cond} + \mathbf{J}_{disp} = \sigma\mathbf{E} + \varepsilon_0 \frac{\partial \mathbf{E}}{\partial t} \tag{4.1}$$

The total current coming out of the probe plate is

$$I = \int_S \mathbf{J} \cdot d\mathbf{S} = \frac{\phi}{R} + C\frac{\partial \phi}{\partial t} \tag{4.2}$$

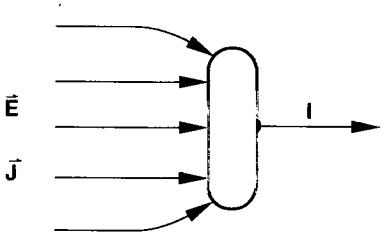

Figure 4.1. *V*-dot detector geometry.

where the resistance is defined as

$$R \equiv \frac{\phi}{\sigma \int \mathbf{E} \cdot \mathrm{dS}}, \tag{4.3}$$

the capacitance is $C \equiv \varepsilon/\sigma R$, and the voltage is

$$\phi = \int_L \mathbf{E} \cdot \mathrm{dl} \tag{4.4}$$

for an electric field over length L. With these definitions Eq.(4.2) can be rewritten as

$$\frac{d\phi}{dt} + \frac{\phi}{RC} = \frac{\phi_0}{R_0 C} \tag{4.5}$$

where ϕ_0 is the signal voltage produced across a calibration resistance R_0, $\phi_0 = IR_0$. The solution to Eq.(4.5) is given by

$$\phi(t) = \frac{1}{R_0 C} e^{-t/RC} \int_0^t e^{t'/RC} \phi_0(t')\, dt' \tag{4.6}$$

The accuracy of Eq.(4.6) depends in large part on how well the parameters R, R_0, and C are known.

Electro-Optic Crystals. The electrically induced birefringence in electrooptic crystals can be used to measure electric fields directly. The experimental arrangement is shown in Figure 4.2. A beam of laser light is directed through an input polarizer whose polarization axis is parallel to the crystal's x–axis. An output polarizer is placed after the crystal as shown. When placed in an electric

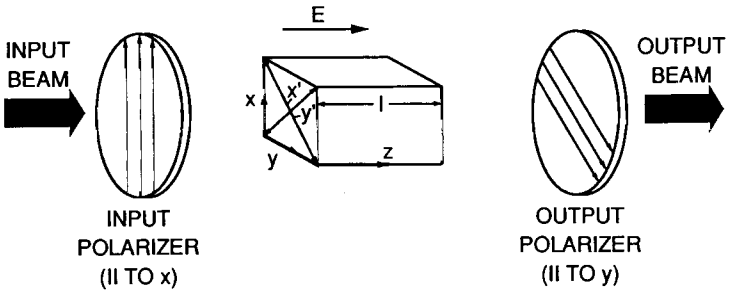

Figure 4.2. Electrooptic-crystal electric field detector.

field E, the crystal experiences a potential drop $\phi = EL$ across its length L. The ratio of the laser light intensity, output to input, is then given by

$$\frac{I_o}{I_i} = \sin^2\left[\left(\frac{\pi}{2}\right)\frac{\phi}{\phi_\pi}\right] \tag{4.7}$$

where ϕ_π is the potential which produces a light retardation of p radians, given by

$$\phi_\pi = \frac{\lambda}{2\, n_0^3\, r_{63}} \tag{4.8}$$

where $\lambda = 2\pi c/\omega$ is the free space wavelength of the laser light, n_0 is the index of refraction of the crystal (typically, 1.5–3.3), and r_{63} is the crystal electrooptic coefficient ($10\text{–}30 \times 10^{-12}$ m/V). For a KD*P crystal, ϕ_π is 3.3 kilovolts. The number of variations measured in I_o/I_i gives the ratio ϕ/ϕ_π, from which the strength of E aligned along the major axis of the crystal can be obtained. Electrooptic crystals find application in laboratory regions where high electric field strengths exist. For example, a 10 kV/m field strength is required to produce ~10^{-3} variation in I_o/I_i.

Spherical Double Probes. Spherical double probes often find application in measuring electric fields in space, where field strengths may be of the order of a millivolt per meter. A spherical double probe consists of two spherical sensors mounted at the ends of wire booms that spin with the satellite as shown in Figure 4.3. The potential difference is measured between the sensors that are typically spaced tens of meters apart. For example, ISEE–1 utilized a 73.5 m probe-to-probe boom length while the GEOS probe-to-probe separation was 42 m (Figure 4.4).

The spherical sensors, each several centimeters in diameter, are constructed of vitreous carbon to ensure uniform work function and photo-emission properties. Unlike magnetic field sensors, probe biasing is necessary to obtain a balance between currents from escaping photo-electrons along the boom with currents from impinging ambient electrons. Often electron guns are necessary for controlling the satellite potential in order to achieve a satisfactory balance.

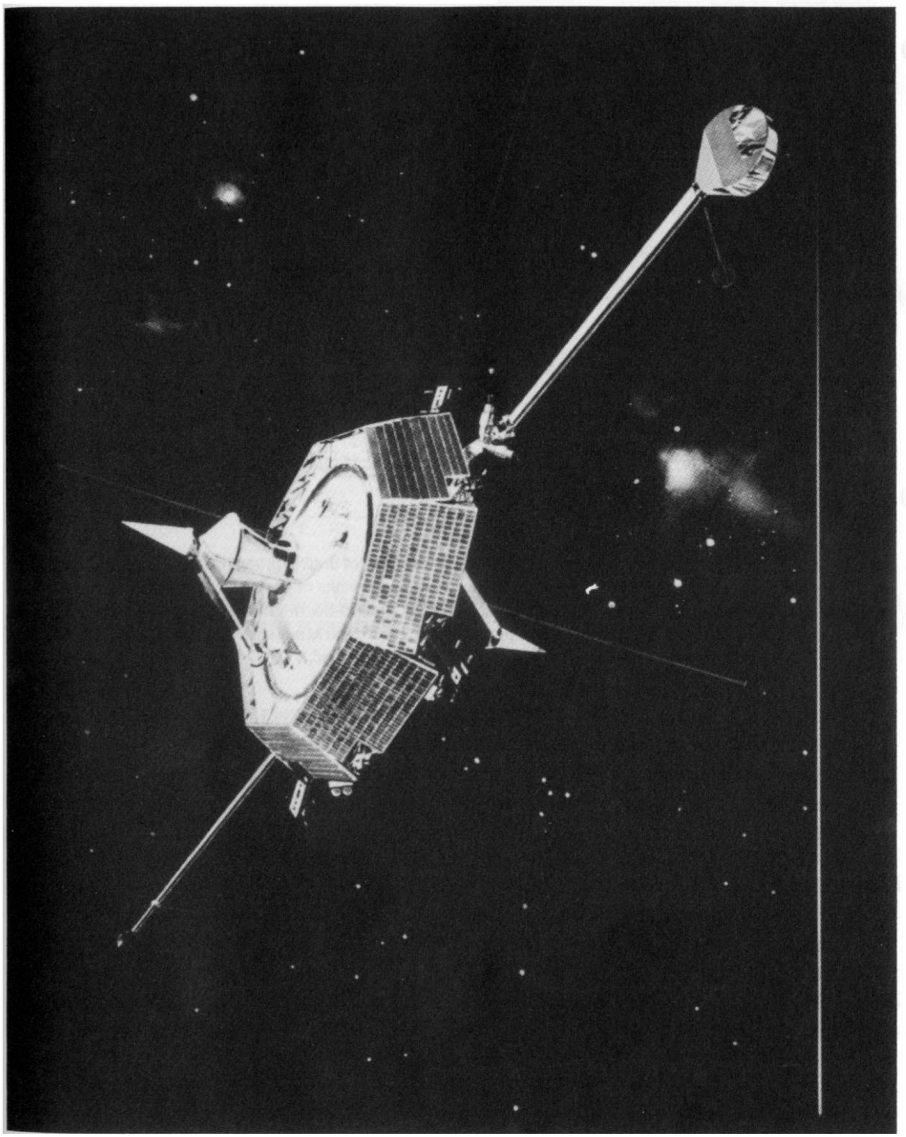

Figure 4.3. The Viking spacecraft with magnetometers and electric field double probes.

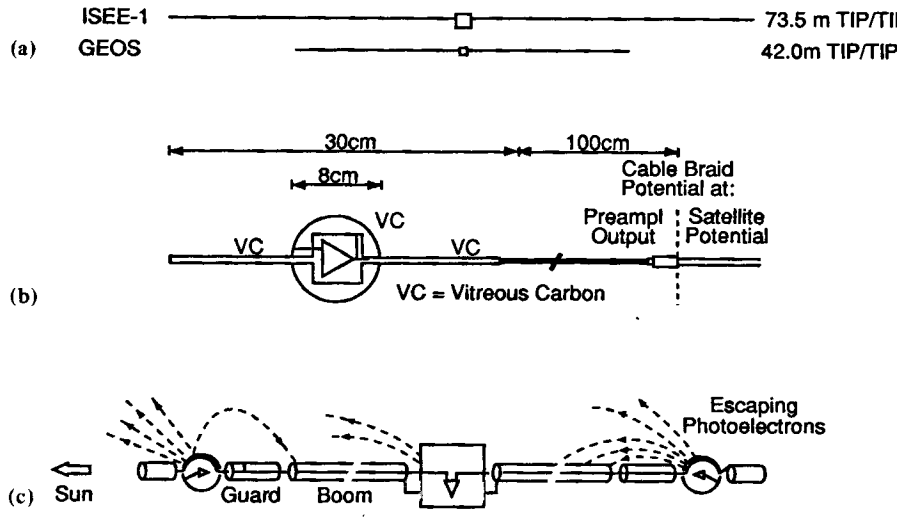

Figure 4.4. Electric field double probes. **(a)** The relative dimensions of double probes on the GEOS and ISEE satellites. **(b)** Sensor arrangement. **(c)** Overall configuration and the paths of photoelectrons which influence the electric field measurements. This figure shows the GEOS–1 guard-boom arrangement. On GEOS–2 the cable braid (100 cm) between probe inner tip and plug could be controlled at negative potentials of a few volts. On ISEE–1 the whole wire boom outer braid potential could be controlled.

In the presence of an electric field, the resulting spin modulation signal between the probes will provide the direction and magnitude of the spin averaged, spin plane component of the electric field. The full electric field vector **E** can be constructed from the measured data under conditions $\mathbf{E}_\perp >> \mathbf{E}_\parallel$.

Ion Detectors. An ion detector in a uniform plasma can measure the bulk velocity components $\mathbf{v}_\parallel$ or $\mathbf{v}_\perp$, parallel and perpendicular to **B**, respectively. In the hydromagnetic approximation the gyrocenter drift is $\mathbf{u}_E = \mathbf{E} \times \mathbf{B}/B^2$, and in a uniform plasma it is $\mathbf{u}_E = \mathbf{v}$. This allows checking of electric field double probe measurements against a plasma experiment (e.g., in the solar wind where $\mathbf{u}_E = \mathbf{v}_\perp$ is the solar wind velocity component perpendicular to the instantaneous magnetic field vector **B**).

Electron Beams. Electron beams emitted from an electron gun may also be used to measure the electric field. The electrons emitted perpendicular to the local magnetic field **B** gyrate around the field and return to their point of origin, provided no other external forces act on them. The actual beam has dispersion causing the electrons to spread in the plane perpendicular to **B**. Their orbits average after each revolution at the point of origin, which acts as a focal point for detection. When an electric field that is perpendicular to **B** is present the electrons undergo a drift motion which results in a shift of the focal point from the origin. This process is identical to the $\mathbf{E} \times \mathbf{B}$ drift of electrons in a magnetron or along a cathode that is magnetically insulated (Figure 4.5).

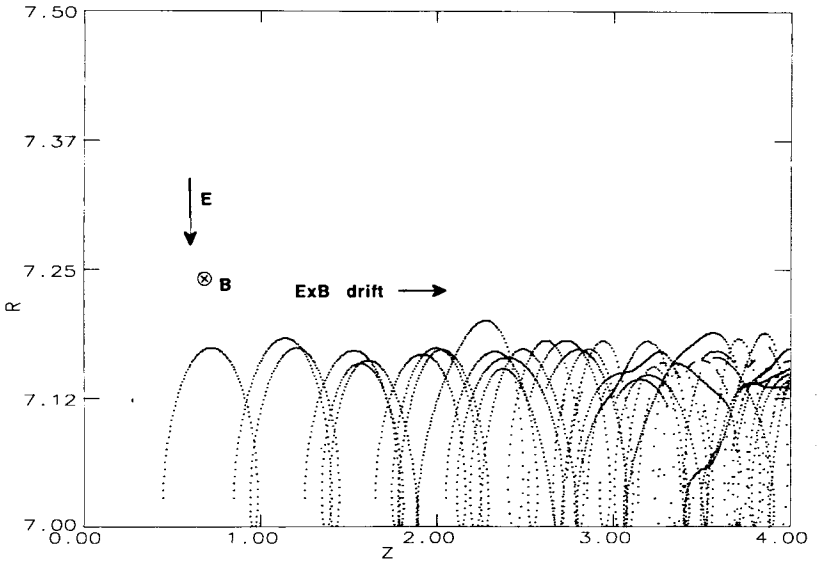

Figure 4.5. Trajectories of electrons in the presence of an electric and magnetic field. The electrons are emitted from a metallic surface located at an arbitrary radius $R = 7.0$.

The displacement perpendicular to the beam s amounts to

$$s = v_{\perp} t_H = \left(\frac{2\pi}{e/m}\right) \frac{E \cos \omega t}{B^2} \tag{4.9}$$

where $v_{\perp}$ is the drift velocity of the electrons perpendicular to the beam, t_H is the gyrotime, and ωt is the momentary angle between E and the direction of the beam. Thus measurement of s and B allows the determination of E through Eq.(4.9)

As an example, for a satellite in stationary orbit about the earth (34,000 km), the magnetic field $B \sim 100\ \gamma$ (100 nT) so that a measured 3 m displacement at the satellite would yield $E \sim 1$ mV/m. The gyroradius is about 1 km, so that the electrons spend most of their flight time away from the satellite and its disturbed surroundings.

4.3 Magnetic Field Aligned Electric Fields

4.3.1 Collisionless Thermoelectric Effect

The average force that a charge carrier experiences from a turbulent time-varying wave field will be different for particles of different energy. In a collision-dominated plasma the friction force

decreases rapidly with energy. This is the ordinary thermoelectric effect, which is capable of supporting a dc electric potential between plasmas of different temperatures without requiring a net electric current. In the classical case we can write the magnetic-field-aligned component of the electric field

$$E_{\parallel} = -\frac{k}{n_e e} T_e^{-\gamma_{th}/2} \frac{d}{ds}\left(n_e T_e^{1+\gamma_{th}/2}\right) \tag{4.10}$$

where γ_{th} is the thermal diffusion coefficient, which has the value 1.4 for singly charged particles in a fully ionized plasma, and d/ds is the derivative along the magnetic field. The thermoelectric field vanishes only if the density n_e and temperature T_e vary in a manner that keeps $n_e T_e^{1+\gamma_{th}/2}$ constant.

4.3.2 Magnetic Mirror Effect

Parallel electric fields supported by the magnetic-mirror force were proposed by Alfvén and Fälthammar (1963) with application to magnetically trapped particles in the absence of net currents. Subsequently, the existence of this mechanism in laboratory plasmas was verified by Geller et al. (1974).

In the case of currents flowing out of the ionosphere, the effect of the magnetic-mirror force becomes particularly pronounced, because the downward flow of current-carrying electrons is inhibited except for those in the loss cone (Figure 4.6).

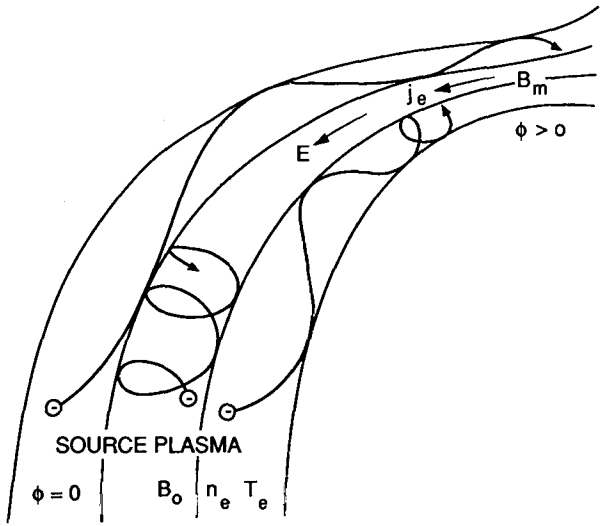

Figure 4.6. The magnetic mirror force restricts the motion of the charge carriers and makes a certain voltage ϕ necessary in order to carry a given current density j_e through the throat of the mirror.

To outline the basic physical characteristics of mirror-supported parallel fields due to upward Birkeland currents, we note that the electron current density $j_\parallel$ at ionospheric altitude is related to the total field-aligned potential drop $\phi_\parallel$ by the relation [Knight 1973, Lemaire and Schere 1974]

$$j_\parallel = en\sqrt{\frac{kT}{2\pi m_e}}\frac{B_i}{B_{\phi\parallel}}\left[1-\left(1-\frac{B_{\phi\parallel}}{B_i}\right)exp\left(\frac{e\phi_\parallel}{kT(B_i/B_{\phi\parallel}-1)}\right)\right] \tag{4.11}$$

where T and n are the electron temperature and density of the magnetospheric source plasma, B_i is the ionospheric magnetic field strength, and $B_{\phi\parallel}$ is the magnetic field strength at the top of the potential variation along field lines. This result will apply provided the electron loss cone in the source plasma is always replenished, otherwise the current can be choked to arbitrarily low values, approaching the idealized case described by Alfvén and Fälthammar. Lemaire and Scherer (1983) have extended Eq.(4.11) to account for both cold and warm electrons as well as ions.

Among the features of Eq.(4.11) is a wide range of voltages for which there is a linear relationship between voltage and current density. It is to be noted that current densities commonly observed above the auroras require potential drops of several kilovolts. Comparisons of the energy flux derived for magnetic-mirror-supported parallel fields to the measured energy flux from rocket flights are in excellent agreement [Lundin and Sandahl 1978].

4.3.3 Electrostatic Shocks

Electrostatic shocks are nonlinear solutions of the coupled time-independent Poisson–Vlasov equations [Eqs.(1.3) and (2.1), in the absence of collisions]. They are characterized by an electrostatic potential jump supported by space charges of electrons and ions in the shock region.

Electrostatic shocks in the magnetosphere are limited regions of strong (several hundred mV/m) transverse electric fields (Figure 4.7).

In earth's magnetosphere electrostatic shocks are reasonably uniformly distributed in local time, with a slight preference for the cusp, and scarcity in the post-midnight (0–6 h) region. Electrostatic shocks have been seen as far out as about 7 R_e. Large shocks occur preferentially

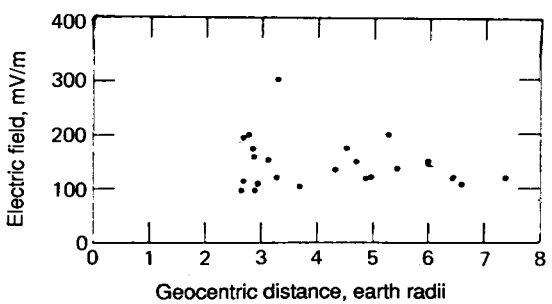

Figure 4.7. Peak electric field strengths in electrostatic shocks observed with ISEE–1. (Courtesy of C.-G. Fälthammar).

above 5,000 km and in the 16–22 h local-time region. However, parallel electric fields related to electrostatic shocks probably extend down below 1,100 km [Mozer 1980]. Upward pointing parallel electric fields of the order of 100 mV/m and extent of 2 km have been measured at an altitude of 7,950 km.

4.3.4 Electric Double Layers

The electric double layer is a thin (tens of Debye lengths) space-charge structure sometimes observed in laboratory experiments of current-carrying plasmas. Between the two sheaths of equal but opposite charges that constitute the double layer there is a strong electric field, but not in the plasma outside it.

The characteristics of the classical double layer are such that for space plasmas electric field strengths as large as 1 V/m are possible. However, this field should have a very narrow altitude range of the order of 100 m, and should therefore be very hard to detect. Instead of a single strong double layer, satellite measurements and numerical simulations reveal the existence of numerous weak double layers, whose total contribution can lead to significant energy gains by the accelerated particles. For example, S3–3 and Viking satellite data indicate that field-aligned potential drops are made up of hundreds or thousands of weak double layers.

Although both wave and dc electric fields can accelerate particles, only a dc field, such as that found in double layers, can accelerate electrons and ions in the opposite directions to about the same energy. Because this mechanism is observed in space, laboratory, and simulation plasmas, in association with strong electric fields, the topic of double layers is covered in detail in Chapter 5.

4.4 Magnetospheric Electric Fields

4.4.1 The Plasmasphere

The plasmasphere is populated by a collision-dominated plasma for which the generalized Ohm's law (Section 2.4.1) can be expected to hold. It is therefore, electrodynamically, the least complicated part of the magnetosphere. At least in the inner parts of this region one would expect a corotational electric field simply mapped from the corresponding areas of the ionosphere. The measurements with GEOS–1 and 2 and ISEE–1 have confirmed this but have also shown interesting deviations. Thus, the average quiet-time electric fields largely agree with what has been expected from Whistler results and theoretical considerations. However, the instantaneous electric field is highly variable and shows considerable deviations from simple corotation. An example of the plasmaspheric electric field is shown in Figure 4.8. Inside 3.3 Earth radii there is a very good agreement with the expected corotational electric field, but further out considerable deviation from corotation are found.

During disturbed conditions, large deviations from corotation are observed near the plasmapause (Figure 4.9). Just inside the dusk side of the plasmapause, electric fields many times stronger than the corotational field, and oppositely directed, have been observed with GEOS–2. During a substorm very strong electric fields were recorded adjacent to and just outside the plasmapause. The field strength projected to the ionospheric level exceeded 100 mV/m, and the

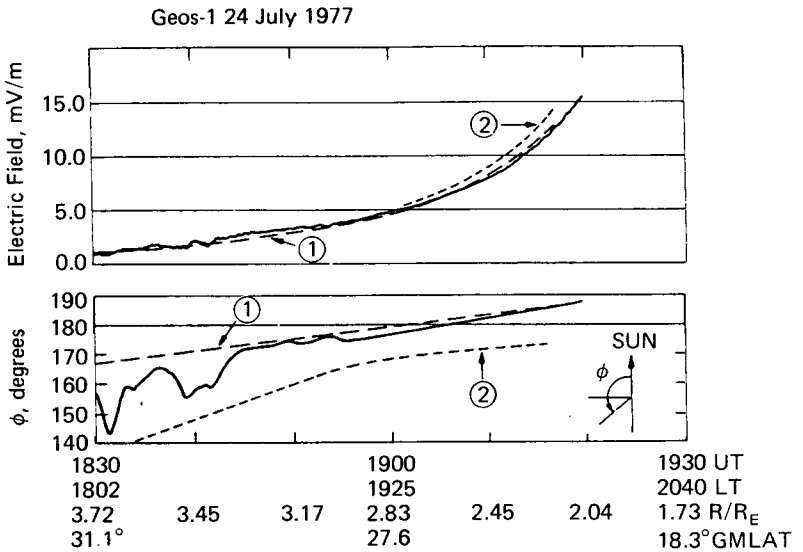

Figure 4.8. Magnitude and direction of GEOS–1 spin plane component of the electric field for an inbound pass through the plasmasphere. Curve 1 is a model field representing perfect corotation. Curve 2 is model field without any corotation. (Courtesy of C.-G. Fälthammar).

event was accompanied by significant penetration of the convection electric field inside the plasmapause.

4.4.2 The Plasmasheet

Unlike a largely homogeneous and steady dawn-to-dusk electric field, the actual electric field in the plasmasheet has proved to be extremely variable, not only in time but also in space. During geomagnetically quiet times the electric field is too weak to be measured with the double probes flown so far (i.e., less than a few tenths of millivolts per meter). Finite small values (0.1–0.3 mV/m) have, however, been measured with the electron beam technique of the GEOS spacecraft.

During the substorm active phase, the electric fields are both strong and variable. As induction electric fields are important during times of extreme variability, there does not even exist an electric potential on the global scale. An example of electric fields measured in the plasmasheet is given in Figure 4.10. Field strengths up to several tens of mV/m have been recorded near the plasmasheet boundary.

Two-point measurements of the electric field components taken by GEOS 2 and ISEE–1 show a time delay between observed pulses (Figure 4.11). The direction of propagation was usually toward the earth with a velocity of the order of the average Alfvén velocity.

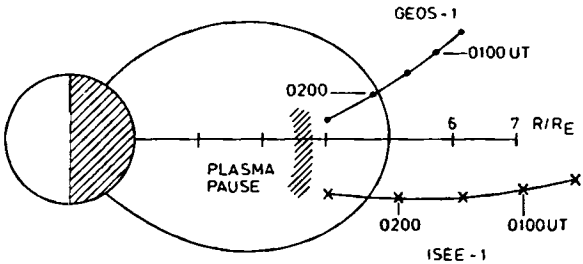

(a)

UT	GMLT GEOS-1	GMLT ISEE-1
0100	0220	0216
0200	0304	0244

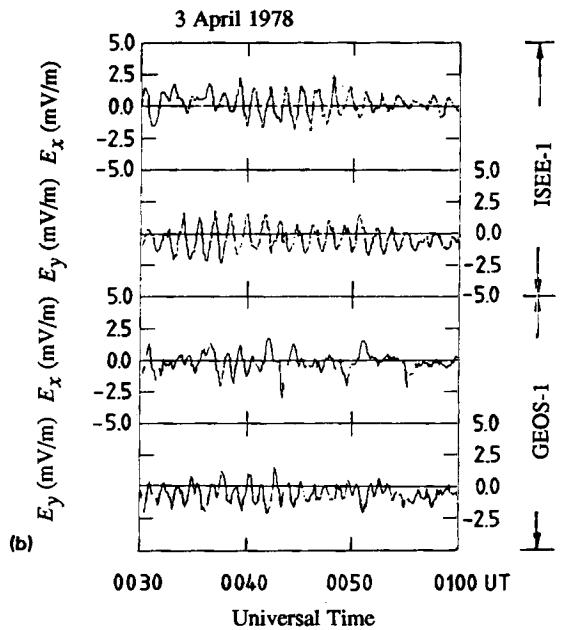

(b)

Figure 4.9. (a) The probe locations and universal times. (b) Comparisons of E_x and E_y during disturbed conditions observed by GEOS–1 and ISEE–1. (Courtesy of C.-G. Fälthammar).

Occasionally, strong electric fields associated with "electrostatic shocks" were seen by ISEE. Figure 4.7 illustrates the peak electric field recorded versus earth radii. As shown, these fields are of the order of a few hundreds of mV/m and extend from 2.5 to 7.5 R_e.

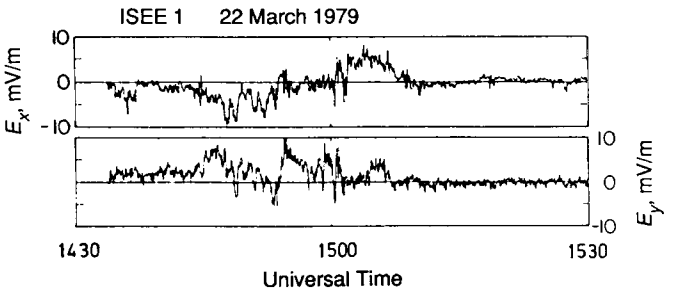

Figure 4.10. The field **E** measured in the plasmasheet during a substorm active phase. (Courtesy of C.-G. Fälthammar).

4.4.3 The Neutral Sheet

At quiet times, the electric field strength in the neutral sheet is typically less than 0.5 mV/m. At active times, the field can reach 6 mV/m (Figure 4.12).

4.4.4 The Magnetotail

Double probe measurements in the central tail lobes have proven unsatisfactory because of low plasma densities. However, in other regions of the tail, measurements have been possible. Information about the electric field have also been drawn from plasma flow detected through anisotropies in measured particle fluxes. One result of the latter kind, is the occurrence of velocity fields with a nonvanishing vorticity (Figure 4.13).

4.4.5 The Magnetopause

Electric fields in the magnetopause are characterized by violent fluctuations with field strengths as high as 10 mV/m. The surprisingly large amplitudes of these fluctuations probably overshadow any dc field that were expected from early models of the magnetopause. Also, the fluctuations are probably important for the penetration of plasma into the magnetosphere, as suggested by several investigators.

4.4.6 The Auroral Acceleration Region

Probably the most interesting electric field observations of all are those made in the auroral acceleration region (Figure 4.14). The first electric field measurements in this region were made with the S3–3 satellite. It led to two major discoveries: "electrostatic shocks" and multiple electric double layers.

Electrostatic shocks with field amplitudes of hundreds of mV/m were measured by S3–3 in the altitude range up to the S3–3 apogee of 8,000 km. Other measurements were made by ISEE–1 and by Viking, which extended the measurement of electric fields up to 13,527 km. An example of the electrostatic shock type observed with Viking is shown in Figure 4.15.

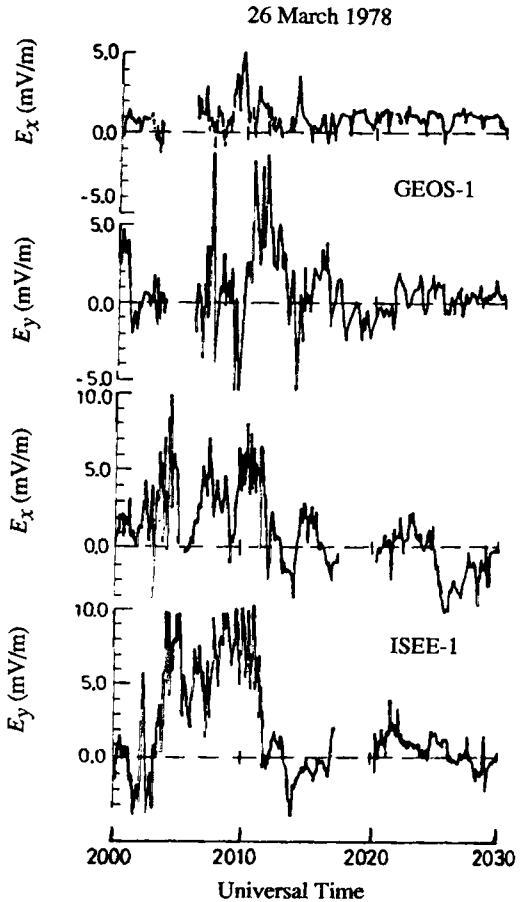

Figure 4.11. Two-point measurements of electric field pulse by ISEE–1 and GEOS–1. (Courtesy of C.-G. Fälthammar).

A typical feature of the Viking electric field data is the prevalence of extremely strong and irregular electric fields above the auroral oval. The occurrence of such electric fields is correlated with regions of electron precipitation. The transition from quiet, several mV/m electric fields at subauroral latitudes to the hundreds of mV/m auroral type oval fields has been found to be very sharp.

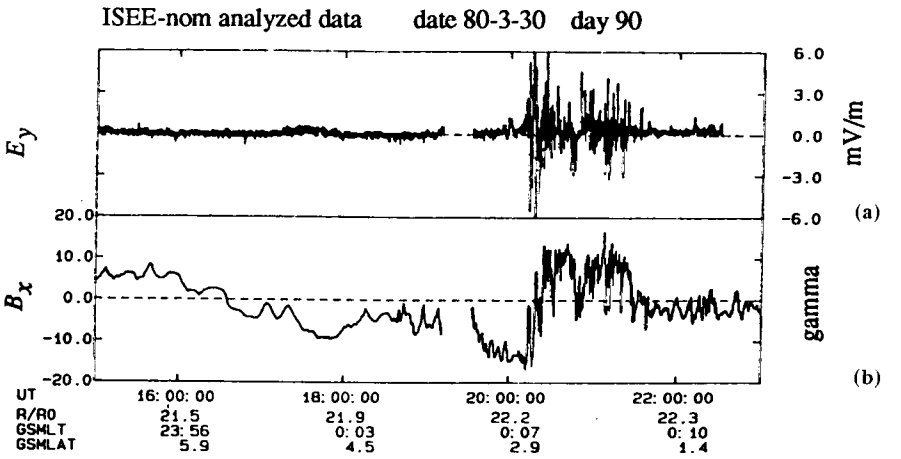

Figure 4.12. (a) Dawn-to-dusk component of the electric field and (b) sunward magnetic field in the neutral sheet. A quiet condition crossing at 16.30 UT with unobservably small electric fields is followed by a disturbed condition crossing in the 20.00 to 21.30 time interval with large and irregular electric fields. (Courtesy of C.-G. Fälthammar).

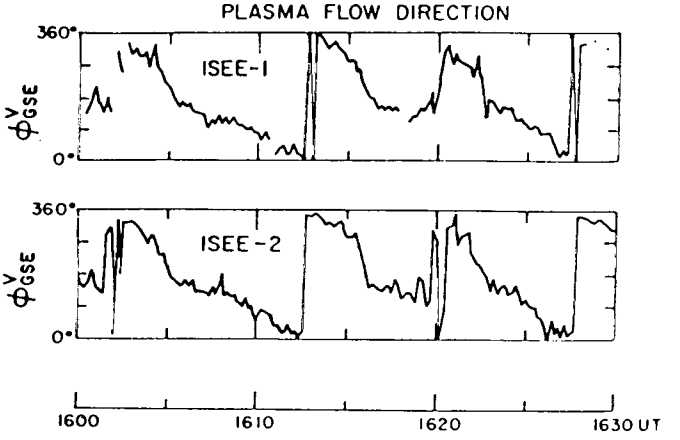

Figure 4.13. The occurrence of velocity fields with a nonvanishing vorticity is shown in this graph taken in the magnetotail. (Courtesy of C.-G. Fälthammar).

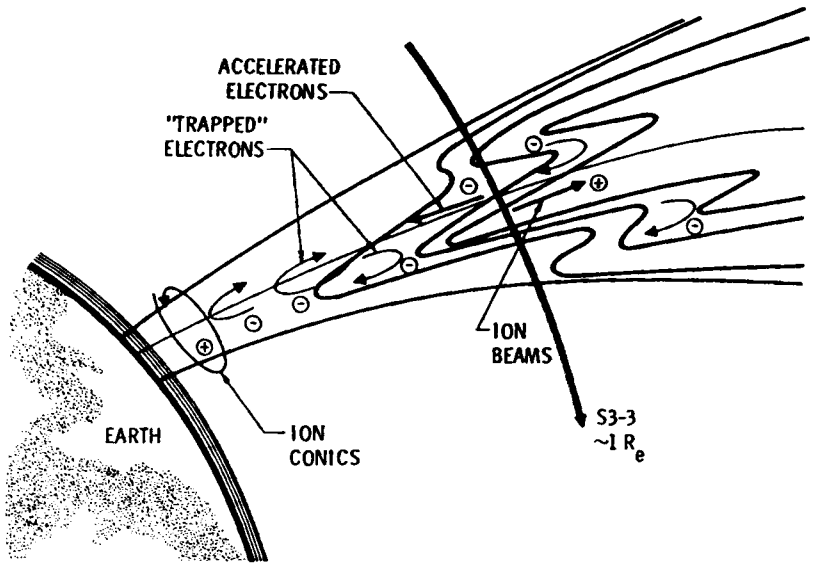

Figure 4.14. Schematic representation of electric equipotentials in the auroral acceleration region.

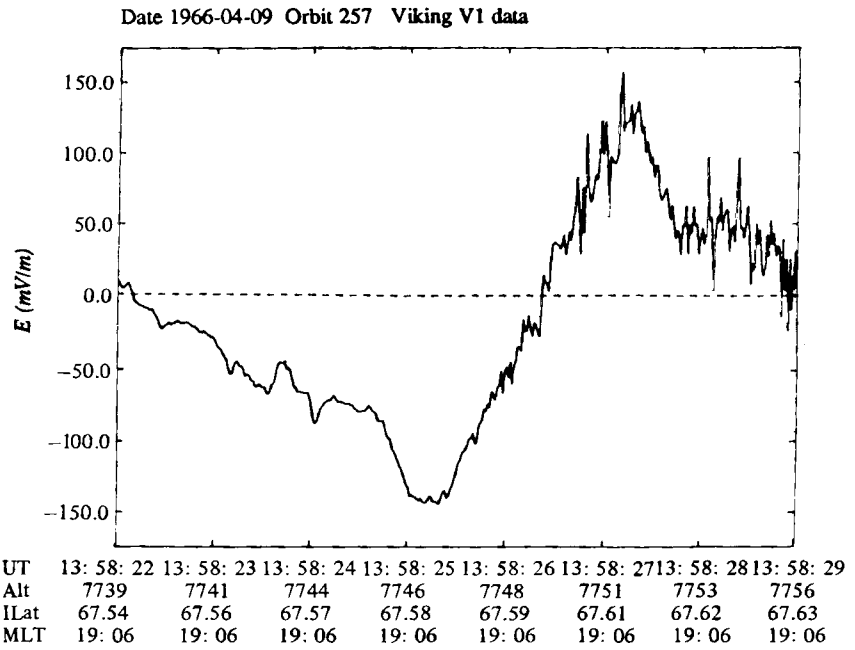

Figure 4.15. Close-up of an electrostatic shock observed with the Viking satellite. The structure of the double electric field spike is shown with enough time resolution to show fine detail. Electric fields with a strength of 150 mV/m are directed inward from both sides. (Courtesy of C.-G. Fälthammar).

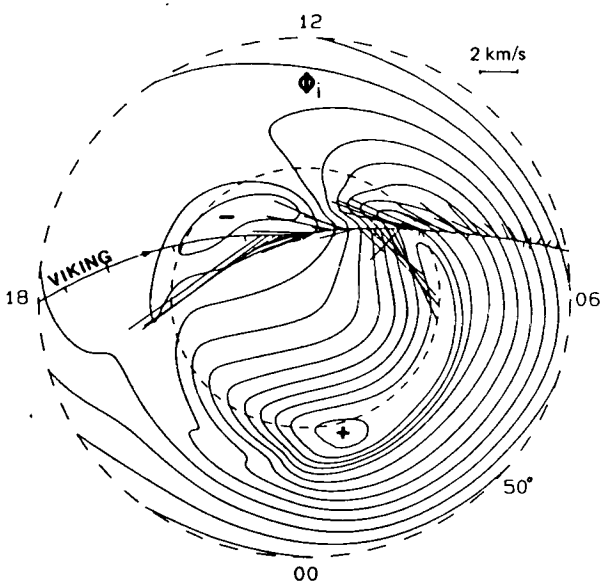

Figure 4.16. Comparison of "instantaneous" global ionospheric potential as calculated with Marklund–Blomberg model and the *in situ* electric field measurements at the Viking spacecraft. For convenience of comparison, the Viking electric field, projected down to the ionosphere, is represented by $\mathbf{E} \times \mathbf{B}$ vectors, which should be tangential to the equipotentials. The equipotentials are given in steps of 5 kV. (Courtesy of C.-G. Fälthammar).

4.4.7 Global Distributions of Auroral Electric Fields

In situ measurements in the magnetosphere have, by necessity, a limited time and space coverage. Measurements are taken along satellite orbits that are traversed at intervals of more than an hour for low orbits, and many hours for high orbits. However by combining (1) *in situ* measurements with (2) remote-sensing information such as the Viking UV pictures of the whole auroral oval, as well as (3) ground-based data relevant to these measurements, and (4) a quantitative mathematical model of the electrodynamics of the auroral ionosphere, rather detailed information can be obtained of the "instantaneous" distribution of auroral electric fields and currents.

Figure 4.16 shows an example of the "instantaneous" global electric potential in the ionosphere as calculated from the Marklund–Blomberg model and the electric field measured *in situ* with Viking and projected down to the ionosphere.[1]

The instantaneous global electric potential pattern calculated by Marklund and Blomberg shows, as it should, a general but not detailed agreement with average patterns calculated for the same geophysical conditions. An example is shown in Figure 4.17. The calculated pattern has also been projected to the equatorial plane and compared to the average plasmapause. The instantaneous demarcation line between open and closed equipotentials of the instantaneous potential distribution shows, as it should, a general but not detailed agreement with the average plasmapause.

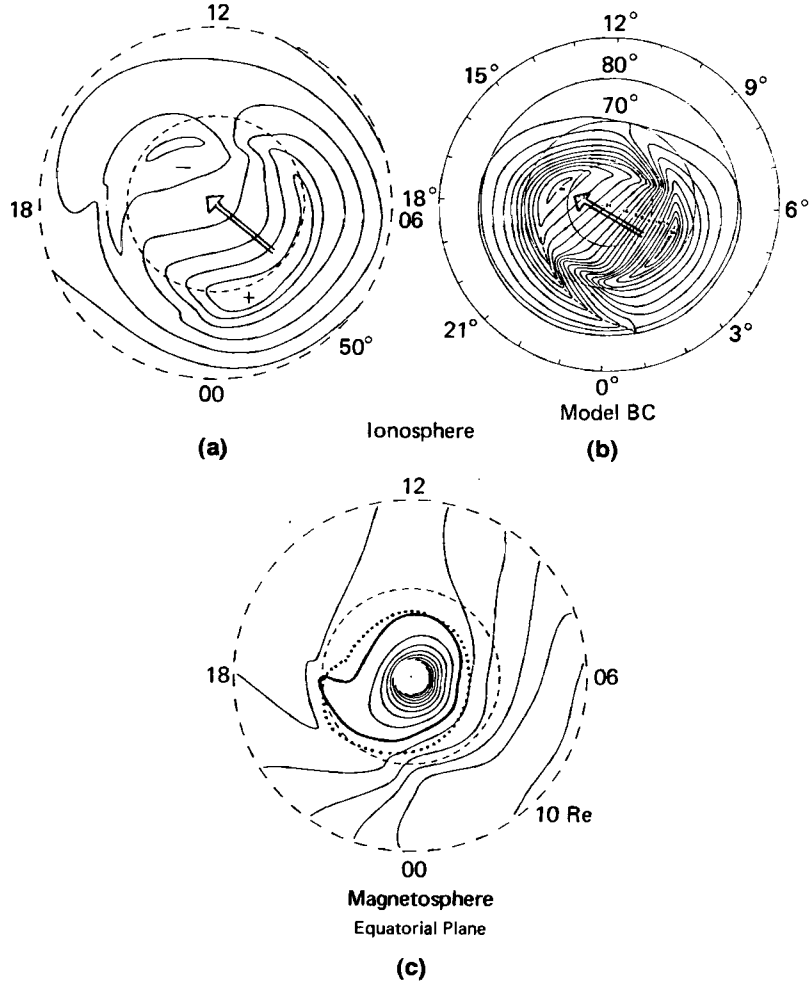

Figure 4.17. Comparison between instantaneous and average potential distributions. **(a)** Instantaneous ionospheric electric potential pattern calculated with the Marklund–Blomberg model. **(b)** Average potential pattern according to Heppner and Maynard (1987) for the same conditions. **(c)** The same pattern projected to the equatorial plane. Also shown, for comparison, is the average plasmapause (heavy line) as deduced from the Whistler data [Carpenter 1966]. (Courtesy of C.-G. Fälthammar).

4.5 Outstanding Questions

The earth's magnetosphere still poses a number of unsolved problems that involve electric fields in a fundamental way. The way in which plasma enters the magnetosphere, both from the solar

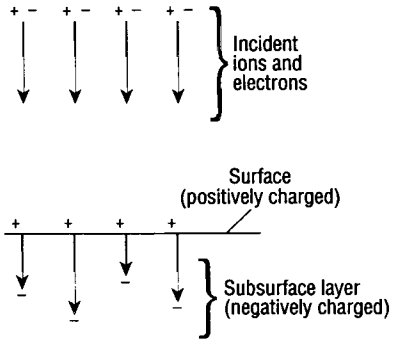

Figure 4.18. A schematic illustration of how a subsurface layer of charged particles forms when a dielectric material is exposed to energetic particles. In general, ions do not penetrate significantly below the surface, but electrons can penetrate to depths ranging from a few micrometers to a few millimeters, depending on their energy and the type of target material. When the electric field that develops between the surface and subsurface layers reaches a critical breakdown value, a surface discharge will occur.

wind and from the ionosphere, is still far from fully understood. More direct measurements are needed to solve the problem of plasma entry.

The earth's own ionosphere is an important source of magnetospheric plasma. The expulsion of ionospheric plasma is the result of complex interactions between the ionosphere and the magnetosphere. In these interactions, electric fields, including magnetic field-aligned electric fields, seem to play an important role.

The auroral acceleration region still holds a number of unanswered questions. They concern, for example, the existence, distribution, and other properties of field-aligned electric fields, and their role in auroral acceleration. These are questions that are also relevant to the understanding of cosmical plasmas in general, which are known to have a remarkable capability of energizing charged particles.

4.6 Phenomena Associated with Electric Fields

4.6.1 Surface Discharges

Surface discharges are produced by large electric fields that develop between the surface and subsurface layers in dielectric materials as a consequence of energetic charged-particle deposition. For example, when spacecraft dielectrics are exposed to bursts of kiloelectronvolt particles during magnetic substorms, the particles penetrate a few micrometers to a few millimeters, building up field strengths which may be of the order of hundreds of kilovolts per centimeter. A schematic representation of this process is shown in Figure 4.18.

If the material is a conductor or a semiconductor, a conduction current will flow in response to the charge deposition and will effectively neutralize the field. If the material is an insulator, the space charge will build up at a rate faster than the local relaxation time, and the associated electric field will increase. When the field reaches a critical value that depends on the material, surface smoothness, and porosity, a surface discharge will occur. This is a problem that often occurs in laboratory pulsed-power and, in fact, is the limiting constraint on how much power can flow in laboratory transmission lines. Figure 4.19 illustrates the "Lichtenstein figures" recorded just below the surface of an acrylic transmission line spacer. Voltage breakdown at dielectric interfaces nearly always results in the formation of these dendrite-type streamers.

Surface discharges will also occur on natural dielectrics in the solar system when these surfaces are exposed to large fluxes of energetic particles. This condition can be found, for example, where magnetospheric currents interact with the surfaces of the giant planets and their satellites.

4.6.2 Plasma Gun Arc Discharges

The plasma gun or dense plasma focus is one of the most "physics-rich" devices in plasma science. Characteristically, it is one of the least understood. The annihilation of magnetized plasma in a pinch results in the collective acceleration of ions to very high energies and the prodigious production of neutrons. In the late 1950s and early 1960s this device saw application in explaining the origin of the planets and satellites [Alfvén 1960, Alfvén and Wilcox 1962]. Today, the dense plasma focus forms one of the most promising alternatives (to Tokamaks) in magnetic fusion [Gratton et al. 1990].

The plasma gun or plasma focus [Alfvén 1958, Lindberg 1960, Lindberg and Jacobsen 1961, Filippov 1962, Alfvén and Fälthammar 1963, Mather 1971, Bostick 1975, Alfvén 1981] is a plasma discharge consisting of a short but finite Z pinch (Section 6.6.1) which forms near or at the end of a coaxial plasma discharge. In the laboratory, the coaxial discharge is formed by switching a charged capacitor bank between a center electrode and an outer conducting tube electrode (Figure 4.20). The discharge is manifested by a current sheath, called a penumbra, that forms between the inner and outer electrodes when the inner electrode is at a positive potential (i.e., an anode) and the outer electrode is at ground (i.e., a cathode). The current sheath is equally-well defined whether the inner electrode is at a positive or negative potential but ion and neutron production at the focus are observed only when the inner electrode is an anode. Part of the stored magnetic energy in the tube and external circuit is rapidly converted to plasma energy during the current sheath's collapse toward the axis. The current flow convergence is largely due to the self-

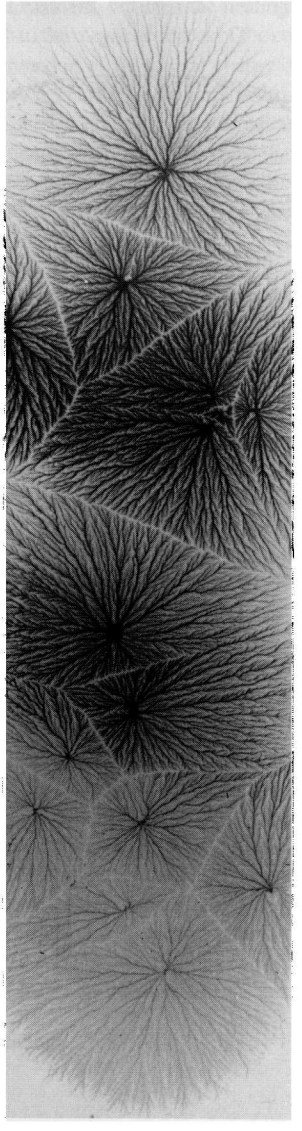

Figure 4.19. Lichtenstein figures recorded on the surface of an acrylic insulator used in a terawatt pulsed-power generator.

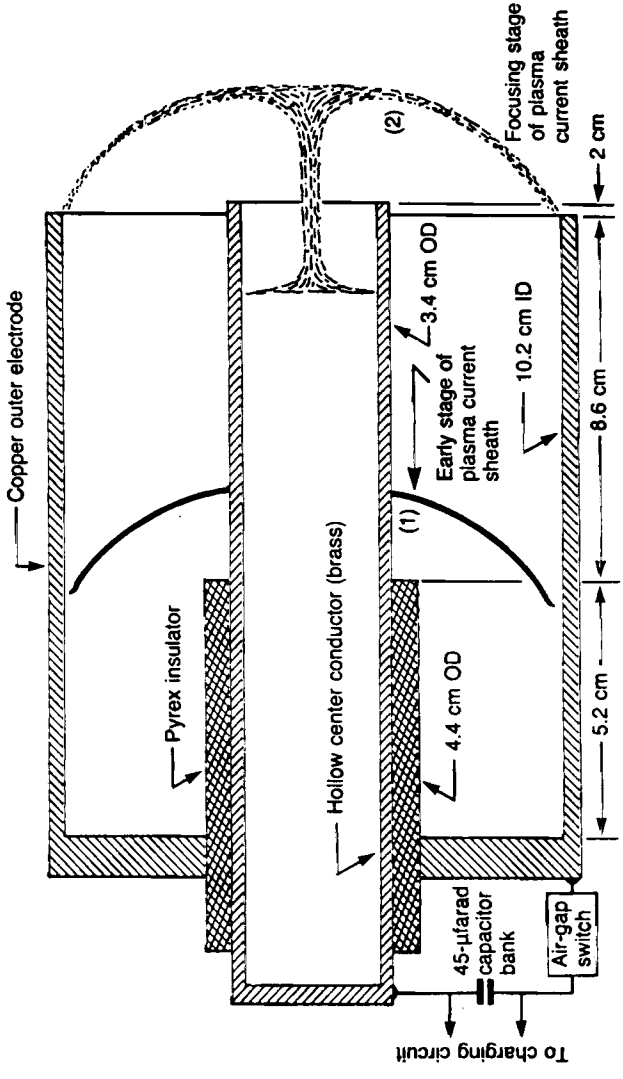

Figure 4.20. Typical plasma gun apparatus. A capacitor bank is discharged through two coaxial electrodes forming a plasma current sheath between inner and outer electrodes. The j×B force accelerates the sheath outward to the ends of the electrodes where the inner sheath radius is forced inwards forming a columnar pinch or "focus" on axis. Also depicted on the diagram is the "penumbra", the long-lived state of the current sheath at the muzzle of the plasma gun. (Courtesy of W. H. Bostick).

constricting nature of the current filament, whereas the heating and compression from the r,z implosion on the axis are due both to the magnetic forces of the current-carrying plasma filament and to inertial forces. Partial conversion of the kinetic energy of the imploding axisymmetric current to internal heat energy may occur during the implosive phase owing to self-collision.

Development of the plasma current leading to the formation of a plasma focus at the center electrode terminus can be conveniently subdivided into three main phases. First is the initial gas breakdown and the formation of a parabolic current front. Second is the hydromagnetic acceleration of a current sheath toward the open end. Third is the rapid collapse of the azimuthally symmetric current sheath toward the axis to form the plasma focus.

Breakdown Phase. The breakdown has a radial, striated light pattern with a definite multifilamentary structure (Figure 4.21). This structure, except for its obvious radial striation, appears cylindrically symmetric (Figures 4.20 and 4.22). As the current increases, the terminus of this visible pattern moves radially outward until it reaches the outer electrode. The current front motion is best described as an unpinch or inverse process [i.e., the $(\mathbf{j}\times\mathbf{B})_r$ body force is exerted outward between the center electrode surface and the plasma current sheath]. During this inverse phase, the sheath remains stable because of the stability of the inverse pinch process (the B_θ lines are convex).

The filamentary structures within the focus, rather than blending together, form a finite number of intense radial spokes ("spider legs"). These spokes appear to retain their identity throughout the acceleration phase and finally coalesce or focus on the axis beyond the end of the center electrode, forming a thin circular annulus (Figure 4.21).

Acceleration Phase. The current sheath across the annulus Δr is not planar, but canted backward from the anode to the cathode owing to the radial dependence of the magnetic pressure gradient. The total acceleration force $\mathbf{j}\times\mathbf{B}$ acting perpendicular to the current boundary leads to radial and axial motion. The $(\mathbf{j}\times\mathbf{B})_r$ radial component is outward and forces the current sheath to be annular at the outer electrode. The axial force $(\mathbf{j}\times\mathbf{B})_z$ varies as r^{-2} across the annulus and leads to higher sheath velocities near the surface of the center electrode. In the laboratory, fast image converter photographs distinctly show a parabolic current front. Owing to the parabolic current boundary, plasma flows centrifugally outward from anode to cathode along the current boundary as the acceleration continues. Plasma is seen to progress radially outward and beyond the outer electrode diameter as the current front accelerates downstream.

The overall time for plasma sheath acceleration to the end of the center electrode is related to the discharge potential across the annulus and the mass density of the background gas. For the case in which the current sheath pushes the gas ahead of the sheath, the sheath velocity is

$$v_s = \left[\frac{E^2}{\mu_0\,\rho_{m0}}\right]^{1/4} \tag{4.12}$$

where E and ρ_{m0} are the discharge field strength and initial mass density, respectively.

Collapse Phase. The third phase encompasses the rapid convergence of the axisymmetric current sheath to the axis and the conversion of stored magnetic energy to plasma energy in the focus. The r,z convergence is due to the $\mathbf{j}\times\mathbf{B}$ pinch force. With this configuration, there is no equilibrium along

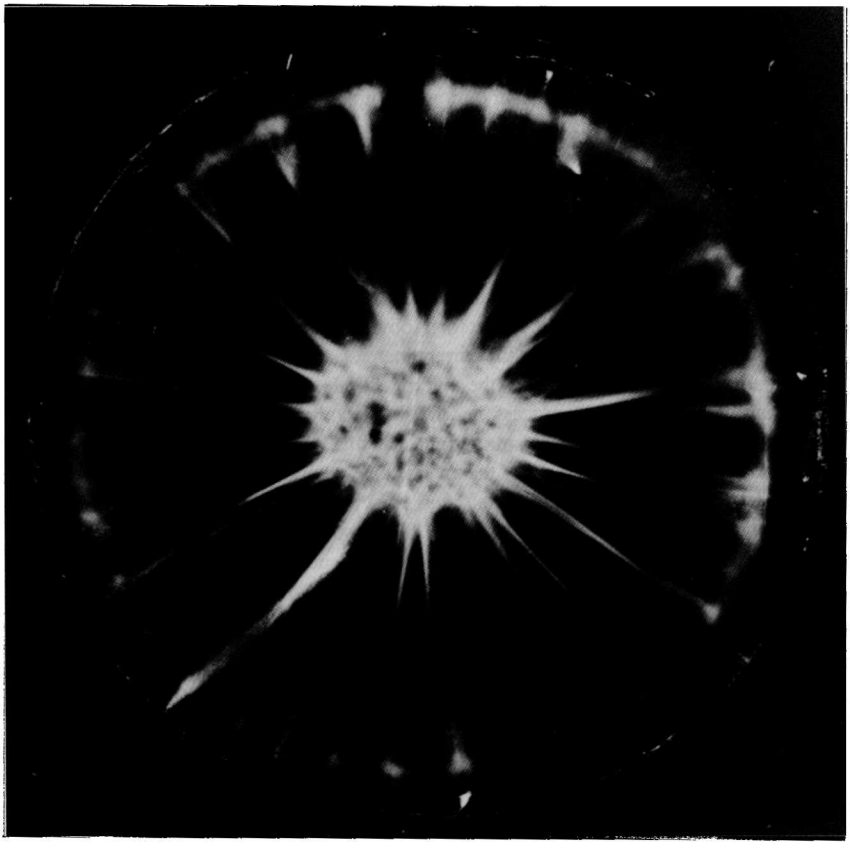

Figure 4.21. End-on recording of the plasma gun penumbra (courtesy of W. H. Bostick).

the axis; hence the plasma may readily escape axially in either direction. By the very nature of the convergence, much of the gas that the sheath encounters during collapse is ejected downstream and lost. The gas trapped in the focus is estimated as ~10% of that originally present.

The pinch effect is perhaps the most efficient way of heating and compressing a plasma. As the pinch induced implosion velocity of the current boundary imparts the same velocity to both ions and electrons, and because of the ion-electron mass difference, most of the energy appears as kinetic energy of the ions. In pinch devices, the ions are preferentially heated.

Dynamic Behavior of the Current Sheath. The dynamic behavior of the plasma current sheath can be analyzed using the measured time dependent values of the voltage $\phi(t)$ across the electrodes, the tube current $I(t)$, and the sheath resistance $R(t)$.

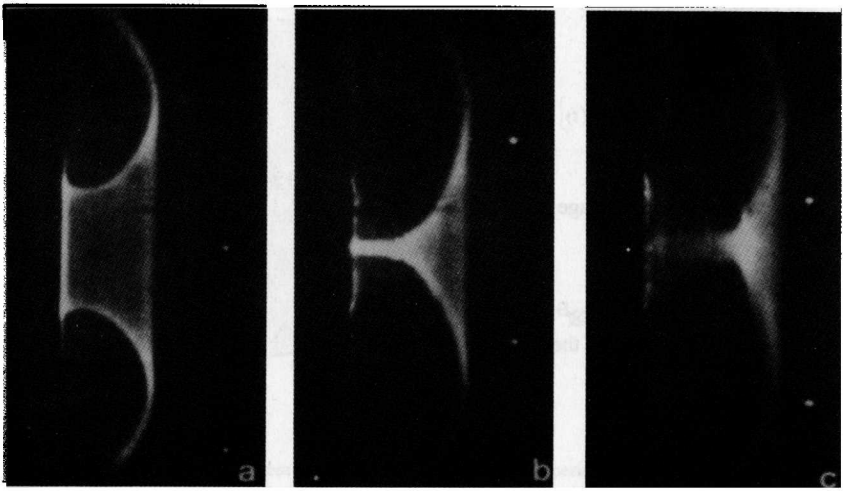

Figure 4.22. Side-on image converter photographs of the plasma penumbra. **(a)** Before columnar collapse or pinch. **(b)** and **(c)** During pinch or "focus".

The circuit equation representing the voltage across the electrodes *ab* in the equivalent electrical circuit (Figure 4.23) is

$$\phi(t) = (d/dt)[L_D(t)\, I(t)] + I(t)\, R_D(t) \tag{4.13}$$

The part of the circuit to the left of *ab* in Figure 4.23 represents the electrical discharge and external circuit resistance R_e and external parasitic inductance L_e. The circuit to the right of *ab* represents the discharge inductance $L_D(t)$ and resistance $R_D(t)$.

Using Eq.(4.13), the following quantities are calculated.

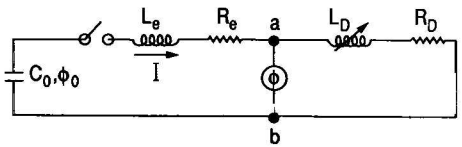

Figure 4.23. Equivalent electrical circuit of the plasma gun discharge. The subscripts e and D denote external and discharge circuit elements, respectively.

(1) Discharge inductance:

$$L(t) = \int_0^{t'} \left[\phi(t) - I(t)\, R(t)\right] dt / I(t) \tag{4.14}$$

(2) Magnetic energy storage Eq.(3.39):

$$W_B(t) = \frac{1}{2}(L_e + L_D)\, I^2 \tag{4.15}$$

(3) Mechanical energy of the sheath:

$$W(t) = \frac{1}{2}\int_0^{t'} \dot{L}_D\, I^2 dt \tag{4.16}$$

where $d/dt(L_D) = \dot{L}_D$ is obtained from Eq.(4.13); and

(4) Pinch voltage during collapse:

$$\phi_p(t) = \dot{L}_D I + I R_D \tag{4.17}$$

The instantaneous mass of the plasma sheath can be estimated using the momentum equation Eq.(2.13) $\rho_m\, \partial \mathbf{v} / \partial \mathbf{t} = \mathbf{j} \times \mathbf{B}$,

$$m_o(t) = \left[10^{-7} \int_0^{t_c} I^2 \ln(r_o / r_i)\, dt\right] v^{-1} \tag{4.18}$$

where $v = v_s$ is the sheath velocity and r_o / r_i the ratio of the outer to inner electrode radii. The upper integration limit t_c is the time to inner penumbra plasma collapse or pinch on axis.

Example 4.1 Electric arcs on the Jovian satellite Io. The satellite Io was observed by the spacecraft Voyager 1 and Voyager 2 to be covered with volcanoes [Morabite 1979, Smith 1979, Strom 1979, Strom and Schneider 1982]. Nine active volcanoes were observed during the Voyager 1 encounter, eight of which were still active during the Voyager 2 flyby four months later. Detailed pictures of the plumes from one of these volcanoes were rather striking in that the plume material was ejected in a well-defined cone whose geometry showed converging (rather than diverging) matter at large lateral distances from the vent, and the plume material was concentrated into striations. Thus, we have a volcanic vent with exit velocities of about 0.5 km/sec, but with the volcanic effluent concentrated into a cone with a half angle initially less than about 25° to the vent axis. Furthermore, the material in the cone tends to concentrate into filaments that terminate on

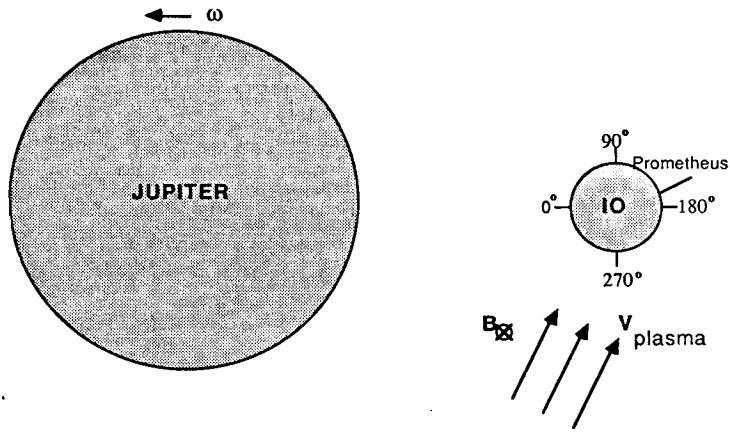

Figure 4.24. The Jupiter–Io system (north pole view). The rotational period of Jupiter is approximately 9^h50^m. The orbital (synchronous) period of Io is 1.770 days. The relative velocity of the plasma torus flowing past Io is 57 km/sec. Io's radius of orbit is 4.22×10^5 km. (Diagram is not to scale).

a narrow, well-defined, concentric annulus [Strom and Schneider 1982]. The possibility that details of the volcanic discharge are a manifestation of a plasma arc at the volcanic vent were initially suggested by Gold (1979).

The dominant electric field in the Jovian magnetosphere is one that is associated with the corotional motion of plasma. This is given by $\mathbf{E} = -(\Delta\boldsymbol{\omega} \times \mathbf{R}) \times \mathbf{B} = -\Delta\mathbf{v} \times \mathbf{B}$, where $\mathbf{R}$ is the position vector from the center of Jupiter and $\boldsymbol{\omega}$ is the angular velocity vector of Jupiter's rotation. The electric field is directed outwards where $\Delta\boldsymbol{\omega} = \boldsymbol{\omega} - \boldsymbol{\omega}'$ is the difference between $\boldsymbol{\omega}$ and the angular velocity $\boldsymbol{\omega}'$ of Io's motion.

Plasma in Jupiter's magnetosphere injected from Io (the Io plasma torus) flows past Io with a speed of about 57 km/sec. The magnetic field from Jupiter at Io is 1900 nT. The $\mathbf{v}\times\mathbf{B}$ voltage induced across Io (3,630 km) is therefore 400 kV, and approximately 10^6 A was observed to be flowing out of the satellite [Acuna et al. 1981, Southwood et al. 1980]. It would seem plausible that the current would tend to concentrate in the volcanic plumes, which would give the current easy access to the highly conducting molten interior of Io. We would suppose that the crust, consisting of sulfur and frozen sulfur dioxide, would be a relatively poor conductor, thus directing the current to the volcanic vents. If we assume the available power (~0.4 TW) is equally divided between the four largest volcanic plumes, we have $\sim 10^{11}$ watts of continuous power available for each volcanic plasma arc. This is roughly equal to the kinetic energy flux of material issuing from a volcanic vent. A small fraction of this power can account for the faint auroral glow reported by Cook et. al. (1981).

Figure 4.24 illustrates the basic geometry at hand. Viewed from the north Jovian and Ionian poles, Jupiter's dipole magnetic field is into the plane of the figure while the plasma flow within the torus is counterclockwise toward Io. With this orientation, the electric field is directed from Jupiter to Io. Volcanic activity on Io generally occurs within an equatorial band of ±30° latitude.

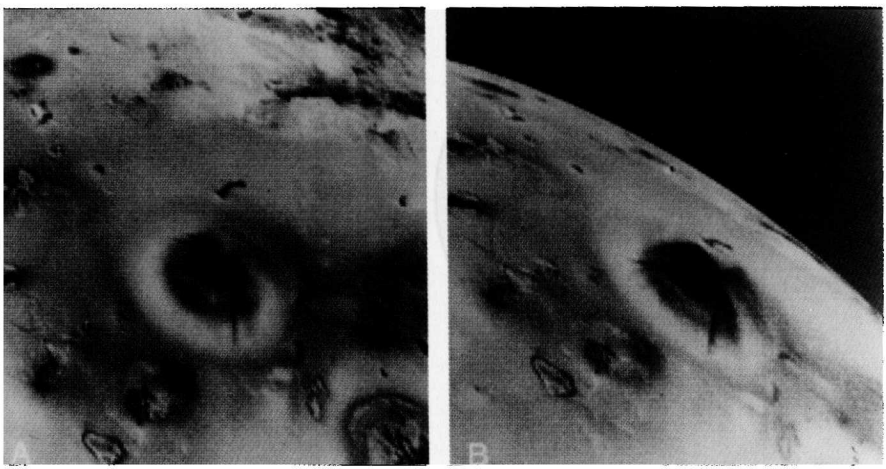

Figure 4.25. Voyager 1 oblique views of Prometheus's plume. The left-hand image was taken 2.3 hours before the right-hand image.

Figures 4.25 and 4.26 are photographs of the particularly well-developed volcanic plume Prometheus (latitude –2.9°, longitude 153°) taken at two different aspect angles by Voyager 1. The height and width of this plume is 77 km and 272 km, respectively [Strom and Schneider 1982] while the vent velocity of the gaseous material ejected is 0.49 km/sec. The current flow is outward from Prometheus (i.e., the vent of Prometheus is an anode). To relate these pictures to the plasma-arc process, we must explicitly assume that the fine particulate matter that makes the volcanic plumes visible is entrained by the plasma. Thus, as the plasma moves to form filaments, we assume that the plasma carries with it the small solid particles.

While an exact calculation of the breakdown field associated with a volcanic arc discharge requires precise knowledge about the region where the breakdown occurs[2], an estimate can be made in the following way [Peratt and Dessler 1988]. For a sufficiently large separation between anode and cathode electrodes, the breakdown field strength in air, nitrogen, freon, and sulfur hexafluoride is [Miller 1982],

$$E_{br}\,(\mathrm{MV/m}) = 2.64\,p\,F^{-1} \tag{4.19}$$

where p is the pressure of the ambient gas in atmospheres and F represents a field enhancement factor of order unity that depends on the shapes of the anode and cathode. Applying Eq.(4.19) to SO_2, the most common gas on Io, while setting $F=1$ and taking an ambient pressure of the gas near the vapor-liquid transition (the triple point for SO_2 is 0.0163 atmospheres), yields $E_{br} = 0.04$ MV/m (0.4 kV/cm). This value is to be compared to the breakdown field strength for lightning on earth [0.44 MV/m (4.4 kV/cm)].

Substituting E=0.04 MV/m and $\rho_{m0} = 2$ gm cm^{-3} into Eq.(4.12), we obtain a parabolic sheath velocity of v_s=0.893 km/sec, close to that observed for Prometheus (0.49 km/s). It is at this

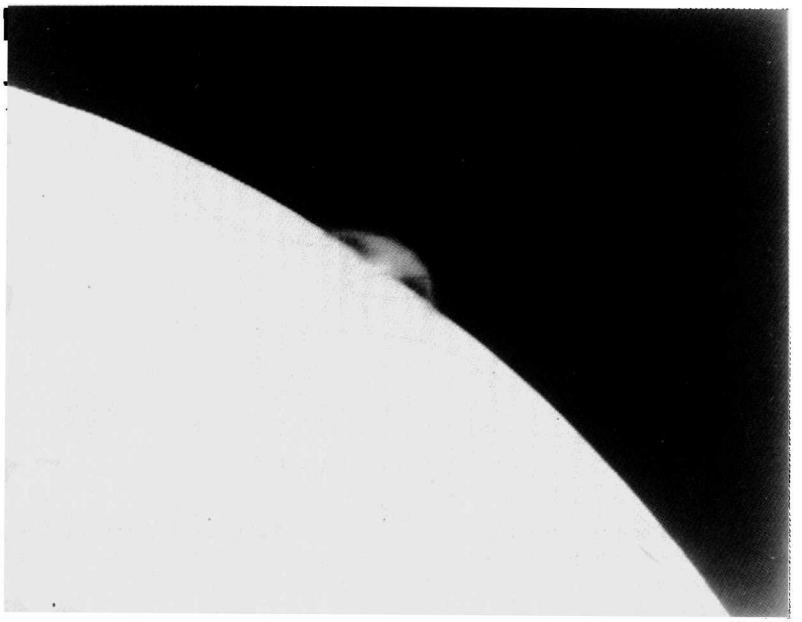

Figure 4.26. Horizon view of Prometheus's plume.

velocity that gas and plasma are pushed into Io's upper atmosphere by means of the arc discharge mechanism. The volcanos effluent is concentrated into a penumbra whose morphology differs from those of ballistic or shock models in two ways. The first is the radial striations resulting from the electromagnetic pinch and accretion of matter into filaments (Figures 4.21 and 4.25). The second is the termination of the penumbra on a narrow cathode annulus (Figures 4.22 and 4.26).

4.6.3 Marklund Convection and Separation of Elements

When an electric field is present in a plasma and has a component perpendicular to a magnetic field, radial inward convection of the charged particles is possible. This situation is depicted in Figure 4.27. Under the influence of the $\mathbf{E} \times \mathbf{B}$ force, both the electrons and ions drift with the velocity

$$\mathbf{v} = (\mathbf{E} \times \mathbf{B})/B^2 \tag{4.20}$$

so that the plasma as a whole moves radially inward. This mechanism provides a very efficient convection process for the accumulation of matter from plasma. The material should form as a filamentary structure about the twisted magnetic flux tubes, the lines of which are commonly referred to as "magnetic ropes" because of their qualitative pattern (Figure 4.28). Magnetic ropes should tend to coincide with material filaments that have a higher density than the surroundings (this is also the case for the filaments in the current sheath of the plasma focus). The cosmic

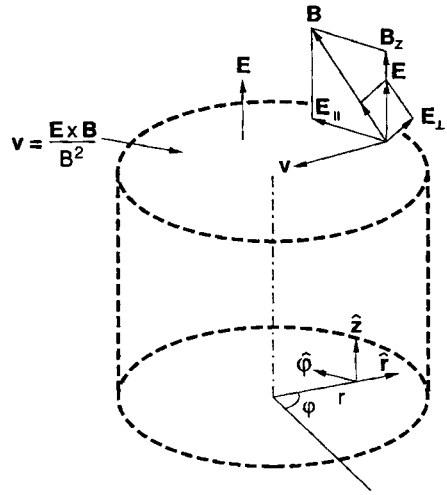

Figure 4.27. When the pressure is negligible the plasma acquires a drift velocity **v** such that the electric field in the moving plasma is parallel to **B**. Therefore, current flows only along the magnetic lines of force.

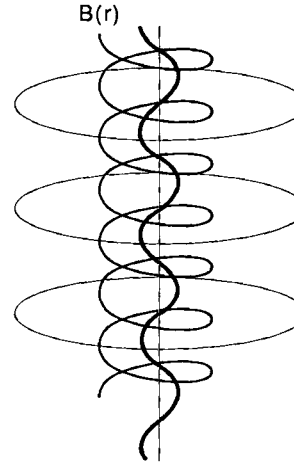

Figure 4.28. A "magnetic rope" with magnetic field lines shown at three different radii.

magnetic flux tubes are not directly observable themselves, but the associated filaments of condensed matter can be observed by the radiation they emit and absorb.

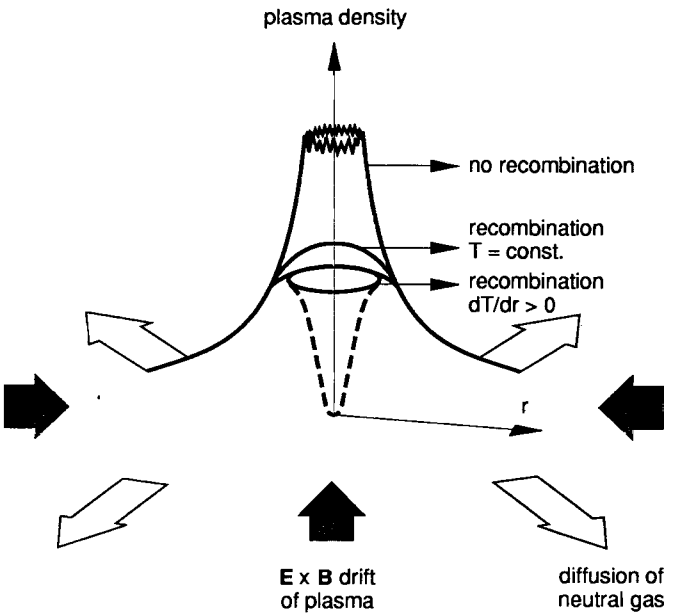

Figure 4.29. Plasma density profile as a function of radius sketched qualitatively for three cases: No recombination, recombination with T = constant, and recombination with a lower central temperature.

When a plasma is only partially ionized, the electromagnetic forces act on the non-ionized components only indirectly through the viscosity between the ionized and non-ionized constituents. From Eq.(4.20), the inward drift of matter is at a velocity $|v_r| \approx E_z / B_\phi$. Hence, at a large radial distance r, the rate of accumulation of matter, per unit length, into a filament is

$$\frac{dM}{dt} = 2\pi r v_r \rho_m = (2\pi r)^2 \rho_m \frac{E_z}{\mu_0 I_z} \tag{4.21}$$

If the electric field is antiparallel to the current, the drift is outwards.

Marklund (1979) found a stationary state when the inward convection of ions and electrons toward the axis of a filament was matched by recombination and outward diffusion of the neutralized plasma (Figure 4.29). The equilibrium density of the ionized component normally has a maximum at the axis. However, because of the following mechanism, hollow cylinders, or modifications of hollow cylinders of matter, will form about the flux tubes.

Because of the radiated loss of energy, the filaments cool and a temperature gradient is associated with the plasma. As the radial transport depends on the ionization potential of the element, elements with the lowest ionization potentials are brought closest to axis. The most abundant elements of cosmical plasma can be divided into groups of roughly equal ionization

potentials as follows: He(24eV); H,O,N(13eV); C,S(11eV); and Fe, Si, Mg(8eV) (Table 1.7). These elements can be expected to form hollow cylinders whose radii increase with ionization potential. Helium will make up the most widely distributed outer layer; hydrogen, oxygen, and nitrogen should form the middle layers, while iron, silicon, and magnesium will make up the inner layers. Interlap between the layers can be expected and, for the case of galaxies, the metal-to-hydrogen ratio should be maximum near the center and decrease outwardly. Both the convection process and the luminosity increase with the field E_z.

For the case of a fully ionized hydrogenic plasma, the ions drift inwards until they reach a radius where the temperature is well below the ionization potential and the rate of recombination of the hydrogen plasma is considerable. Because of this "ion pump" action, hydrogenic plasma will be evacuated from the surroundings and neutral hydrogen will be most heavily deposited in regions of strong magnetic flux.

Examples of this convection for galaxies are given in Section 3.11.3. In addition, Mirabel and Morras (1984) have detected the inflow of neutral hydrogen towards our own galaxy.

4.6.4 Particle Acceleration and Runaway

The equation of motion of an electron in a region of plasma in which there is an external electric field **E** is [c.f. Eq.(C.1)]

$$m_e \dot{\mathbf{v}} = -e\,\mathbf{E} - \nu_c m_e \mathbf{v} \tag{4.22}$$

where ν_c is the electron-electron collision frequency associated with the so-called dynamical friction from Coulomb scattering [Rose and Clark 1961], given by

$$\nu_c = \frac{e^4 n_e \ln \Lambda}{2\pi \varepsilon_0^2 m_e^2 \mathrm{v}^3} \tag{4.23}$$

where

$$\Lambda = \frac{12\pi (\varepsilon_0 k T / e^2)^{3/2}}{n_e^{1/2}} \tag{4.24}$$

Considering only the case of electron velocities along the electric field, we may utilize the scalar form of Eq.(4.22) and write

$$\dot{\mathrm{v}} = \frac{e}{m_e} E - \frac{e^4 n_e \mathrm{v} \ln \Lambda}{2\pi \varepsilon_0^2 m_e^2 \mathrm{v}^3} \tag{4.25}$$

Equation (4.25) is the dual of the sum of a uniform field plus the field of a point charge.

To gain some insight into the meaning of Eq.(4.25), consider two electrons, one with initial velocity $\mathrm{v}(0)$ small and the other with initial velocity $\mathrm{v}(0)$ large. For the former, if

$$v(0) < v_{crit} = \left[\frac{e^3 n_e \ln \Lambda}{2\pi \varepsilon_0^2 m_e E}\right]^{1/2} \tag{4.26}$$

the right-hand side of (4.25) is negative and the electron eventually decelerates to a stop. For the latter, $v(0) > v_{crit}$, and the electron accelerates. Since Eq.(4.23) decreases with the inverse cube of the velocity, the drag force decreases as the electron accelerates, causing the electron acceleration to increase still further.

This phenomenon is known as *electron runaway*. Electrons with an initial velocity above the threshold velocity gain speed indefinitely (within the limits of relativity), so long as the electric field is present, and "run away", while initially slow electrons come to rest.

To determine what portion of an electron population undergoes runaway, we rewrite the critical velocity Eq.(4.26) in form of the kinetic energy

$$\frac{m_e v_{crit}^2}{2e} = \frac{e^2 n_e \ln \Lambda}{4\pi \varepsilon_0^2 E} = 2.6\times10^{-17} \frac{n_e \ln \Lambda}{E} \quad \text{eV} \tag{4.27}$$

We note that the threshold velocity equals the electron thermal velocity v_{the} for a field

$$E = E_D = \frac{e^3 n_e \ln \Lambda}{2\pi \varepsilon_0^2 m_e v_{the}^2} = \frac{e^3 n_e \ln \Lambda}{2\pi \varepsilon_0^2 kT} \tag{4.28}$$

This field is called the *Dreicer field*. In terms of the E_D, the critical velocity is

$$v_{crit} = v_{the}\left(\frac{E_D}{E}\right)^{1/2} \tag{4.29}$$

so that large fields E imply low v_{crit} and a large population of runaway electrons.

Example 4.2 Runaway electrons in fusion and cosmic plasmas. Consider a fusion plasma $n_e=10^{20}$ m^{-3}, E=10 V/m, and ln Λ = 20. Substituting these values into Eq.(4.27) shows that electrons with energies above 5 keV will run away. Consider a cosmic plasma $n_e=10^3$ m^{-3}, $E=10^{-6}$ V/m, and T=3 keV. For these values, electrons with energies greater than 0.5 micro-electronvolts will run away. Thus, electrons in cosmic plasmas are readily accelerated to high energies in the presence of even very small electric fields.

Equation (4.22), and the runaway process, will be modified if a magnetic induction **B** is present. However, if **E** and **B** are parallel, the runaway condition is not altered. In addition, the body of electron population which attracts electrons of less than runaway speed is eroded by the escape of electrons brought up to critical speed. If the electric field persists long enough, all the electrons will eventually run away in energy.

4.6.5 Field-Aligned Electric Fields as the Source of Cosmic Rays

Cosmic rays are extraordinarily isotropic on earth, having a degree of anisotropy of about 0.1 for low energy particles, then decreasing to $\pm 5 \times 10^{-4}$ for particles approaching energies of 10^{20} eV. At one time, it was generally believed that cosmic rays were born in the shock waves produced by supernovae. However, it is now realized that the degree of anisotropy that would be produced by such shocks is far larger than that observed.

Example 4.3 The anisotropy of charged particle fluxes from supernovae produced shock waves. Consider the number of supernovae in our Galaxy capable of subtending a cone of cosmic ray flux of solid angle $(D / R_{gal})^2$ on earth where $D \sim 10^2$–10^3 pc is the size of the shock accelerating medium and $R_{gal} \sim 10^4$ pc. This number is

$$N_{sn} = f_{sn}\, \tau_{sn}\, (D / R_{gal})^2$$

where the frequency of supernovae events is $f_{sn} \sim 1/100$ yrs, and the duration $\tau_{sn} \sim 10^7$ yrs. Thus, $10 \leq N_{sn} \leq 500$ and the degree of anisotropy defined by $an \equiv (2 N_{sn})^{-1/2}$ is large, $0.03 \leq an \leq 0.3$.

Colgate (1990) points outs that because of the high anisotropy of any shock wave acceleration together with the complete lack of any laboratory evidence that shock-wave/charge particle acceleration actually exists, that field-aligned electric fields are the most plausible mechanism for producing cosmic rays. This mechanism is addressed in Section 5.6.4.

Notes

[1] To facilitate comparison, the Viking electric field is represented by means of the $\mathbf{E} \times \mathbf{B}$ vectors, which should be tangent to the electric potentials.

[2] Comparison of the side-on penumbra morphology (Figures 4.20 and 4.22) to the side-on plume morphology (Figure 4.26) suggests that the location of the electrical discharge may be well below the surface of Io.